THE ASTROPHYSICAL JOURNAL, 456:337–349, 1996 January 1

MODELING OF THE DUST AND GAS OUTFLOWS FROM OH 26.5+0.6: THE SUPERWIND

K. JUSTTANONT,[1,2] C. J. SKINNER,[3,4] A. G. G. M. TIELENS,[1] M. MEIXNER,[5] AND F. BAAS[6,7]
Received 1995 April 7; accepted 1995 July 6

ABSTRACT

We have observed the extreme OH/IR star, OH 26.5+0.6, in the infrared dust continuum and in the submillimeter rotational lines of CO. Mid-infrared images reveal the compact nature of the circumstellar shell (<0.″5). A deep 9.7 μm absorption feature and an absorption at 18 μm show that the dust mass-loss rate is very high. However, the low antenna temperatures of CO $J = 1$–0 and 2–1 lines suggest that the outer part of the circumstellar shell is much more tenuous. In order to resolve this discrepancy, we have observed the $J = 3$–2 and 4–3 CO rotational transitions.

We have developed a model for the circumstellar shell for OH 26.5+0.6 which is consistent with the infrared and submillimeter observations. The dust and gas data are well fitted by a two-shell model, consisting of a dense shell surrounded by a more tenuous shell. The former we identify with the superwind ($\dot{M} = 5.5 \times 10^{-4}$ $M_\odot$ yr^{-1}), and the latter we identify with mass loss on the asymptotic giant branch (AGB) ($\dot{M} = 10^{-6}$ $M_\odot$ yr^{-1}). The transition between the two mass-loss phases is shown to be rather abrupt ($\Delta t < 150$ yr). Depending on the mass of the progenitor, this superwind phase may be the last thermal pulse (for $M_* < 1.5$ $M_\odot$), or the first of a series of the superwind phases (for up to 8 $M_\odot$), punctuated by a period of low mass-loss rates, before the star evolves off the AGB.

Subject headings: circumstellar matter — dust, extinction — infrared: stars — stars: AGB and post-AGB — stars: individual (OH 26.5+0.6) — stars: mass loss

1. INTRODUCTION

When a star is on the asymptotic giant branch (AGB), it becomes unstable against pulsation and loses mass. The gas flowing away from the central star cools, and dust grains can condense out when the temperature falls below the specific condensation temperature for that dust species. For O-rich stars, condensates are silicates, while for C-stars, SiC and amorphous carbon are observed in the outflow. As a result, the star becomes heavily obscured by its dust shell, and the spectral energy distribution peaks in the infrared. Some O-rich AGB stars exhibit OH masers and are called OH/IR stars (Wilson & Barrett 1972). The lifetime of the AGB phase is thought to be a few 10^5 years, during which the star has shed much of its envelope before evolving into a planetary nebula (Iben & Renzini 1983). It is not clear whether mass loss in the AGB stage increases slowly with time (Baud & Habing 1983), whether it increases abruptly at the end of the AGB in the form of a superwind (Renzini 1981), or whether mass loss is interrupted many times (Olofsson et al. 1990; Waters et al. 1994).

During the AGB phase, stellar evolution is determined by mass loss rather than nuclear burning (Schönberner 1983; Weidemann & Koester 1983). Hence, understanding the mass-loss process and its dependence on stellar parameters forms the key to understanding the ultimate fate of low- and intermediate-mass stars. In recent years, it has been recognized that mass-loss rates determined from dust and gas observations show large discrepancies for extreme OH/IR stars (Heske et al. 1990; Justtanont, Skinner, & Tielens 1994).

Dust mass-loss rates can be calculated by modeling mid-infrared energy distributions of these stars (e.g., Jones & Merrill 1976; Rowan-Robinson & Harris 1983; Bedijn 1987; Justtanont & Tielens 1992; Griffin 1993). In particular, the strength of the 9.7 μm silicate emission or absorption feature correlates well with the mass-loss rate (Skinner & Whitmore 1988; Schutte & Tielens 1989). For extreme OH/IR stars, such as OH 26.5+0.6, the observed deep 9.7 μm silicate absorption feature implies dust mass-loss rates of $\sim 10^{-6}$ $M_\odot$ yr^{-1}, corresponding to a gas mass-loss rate of $\sim 10^{-4}$ $M_\odot$ yr^{-1}. CO has been used successfully to estimate gas mass-loss rates in late-type stars (e.g., Knapp et al. 1982; Knapp & Morris 1985). The latter authors studied 50 AGB stars and obtained an empirical formula for calculating mass-loss rates. A catalog of CO submillimeter observations has been compiled by Loup et al. (1993). Many of the extreme OH/IR stars have been detected in CO 1–0 and 2–1 lines (Heske et al. 1990). However, the measured antenna temperatures for both lines are very low, implying low gas mass-loss rates ($\sim 10^{-6}$ $M_\odot$ yr^{-1}). It is possible that these stars have just entered ($\leq 10^3$ years ago) a superwind phase and the enhanced density seen in the infrared has not reached the outer part of the envelope, which results from the earlier epoch of low mass-loss rate.

Justtanont et al. (1994) made a study of one such source, OH 26.5+0.6, in which the superwind-AGB mass-loss model has been used to calculate the CO outflow from the star. In order to test these models, we have obtained observations of higher rotational transition of CO and mid-infrared images of this source. This information, coupled with the mid-infrared spectroscopy, has given more constraints for our model. All the observations are described in § 2. Models for the circumstellar

[1] NASA Ames Research Center, MS 245-3, Moffett Field, CA 94035.
[2] Institut d'Astrophysique de Paris, 98 bis, Boulevard Arago, 75014 Paris, France.
[3] Space Telescope Science Institute, 3700 San Martin Drive, Baltimore, MD 21218.
[4] Institute of Geophysics and Planetary Physics, Lawrence Livermore National Laboratory, P.O. Box 808, Livermore, CA 94581-9900.
[5] Astronomy Department, MC 221, 1002 W. Green Street, University of Illinois, Urbana, IL 61801.
[6] Leiden Observatory, P.O. Box 9513, NL-2300, RA Leiden, The Netherlands.
[7] Joint Astronomy Center, 660 N. A'ohoku Place, University Park, Hilo, HI 96720.

shell of OH 26.5+0.6 are discussed in § 3. Our infrared and submillimeter results are reported in §§ 4 and 5, with the conclusion in § 6.

2. OBSERVATIONS

The spectroscopy at 10 and 20 μm was carried out on UKIRT using the Cooled Grating Spectrometer 3 (CGS3). The spectrometer contains an array of 32 discrete As:Si photoconductive detectors and three interchangeable permanently mounted gratings covering the 10 μm and 20 μm atmospheric windows. Two grating settings give a fully sampled 64 point spectrum of the chosen wave band. The 10 μm low-resolution grating covers the wavelength range 7.4–13.3 μm with a resolution of 55. The 20 μm grating covers the range 15.4–24.1 μm with a resolution of 74. The aperture was set at 5″.5. The 10 μm spectrum was taken in 1990 July, while the 20 μm data were taken in 1991 May. The spectra are shown in Figure 1.

The narrow-band ($\Delta\lambda/\lambda = 10\%$) mid-infrared images of OH 26.5+0.6 were taken with the Berkeley/LLNL mid-infrared array camera (Arens et al. 1987; Keto et al. 1992) at UKIRT on 1992 June 1 (8.0 and 10.0 μm) and at the IRTF on 1991 August 2 (12.5 μm). Standard nod and chop procedures described by Ball et al. (1992) were used for sky subtraction. Flat-fielding of the images was achieved by using dark subtracted sky frames that are normalized to the mean (Meixner 1993). The pixel scales were 0″.39 for all observations, resulting in a field of view of 3″.9 × 25″. Each image of OH 26.5+0.6 and of the standard star, γ Aql, resulted from three panel mosaics along the short axis of the chip. Exposures in each of these panels were stitched together using an automatic registering program based on a minimum least-squares criteria for matching the pieces. Errors in the images from this mosaicking program are less than one-fifth of a pixel. Flux calibration was derived from fluxes of γ Aql determined by Cohen et al. (1995). Final total fluxes for OH 26.5+0.6 are 274, 174, and 174 Jy at 8, 10, and 12.5 μm. Note that 12.5 μm was taken almost a year earlier. Images of both OH 26.5+0.6 and γ Aql for all three wavelengths are shown in Figure 2.

CO $J = 3$–2 and 4–3 observations were obtained in 1993 May with the 15 m JCMT, using receivers B3(i) and C2(i) at the rest frequencies of 345 and 461 GHz. The frequency resolution for both is 1.2 MHz. The beamwidths are 15″ and 11″ for $J = 3$–2 and 4–3 transitions. The main beam efficiencies are 0.54 and 0.46, respectively. The system temperature for the 345 GHz receiver is 850 K, and it is 6000 K for the 461 GHz receiver. We used the H II region G34.3 to check our flux calibration for both frequencies. Owing to the interstellar contamination in the line of sight to OH 26.5+0.6, we position switched in declination with a throw of 16′.7 for both transitions. However, a contaminating interstellar component is still present in the $J = 3$–2 profile. The observed line profiles are shown in Figure 3.

3. MODEL OF THE CIRCUMSTELLAR ENVELOPE OF OH 26.5+0.6

OH 26.5+0.6 is an extreme OH/IR star with a very high dust mass-loss rate which renders the star optically invisible. It has been studied at various wavelengths, spanning from the

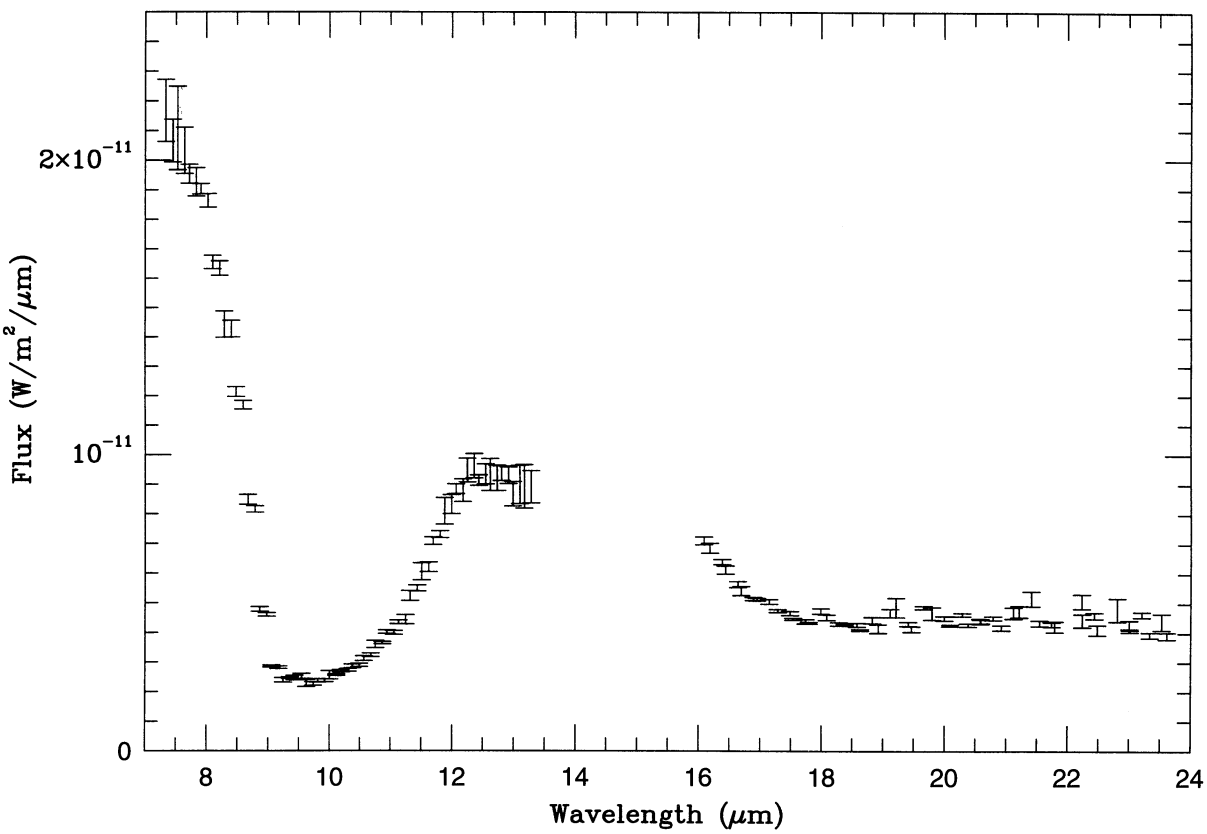

FIG. 1.—The 10 and 20 μm spectroscopy of OH 26.5+0.6 using CGS3. The flux level has been adjusted so it coincides with the *IRAS* photometry point at 12 μm.

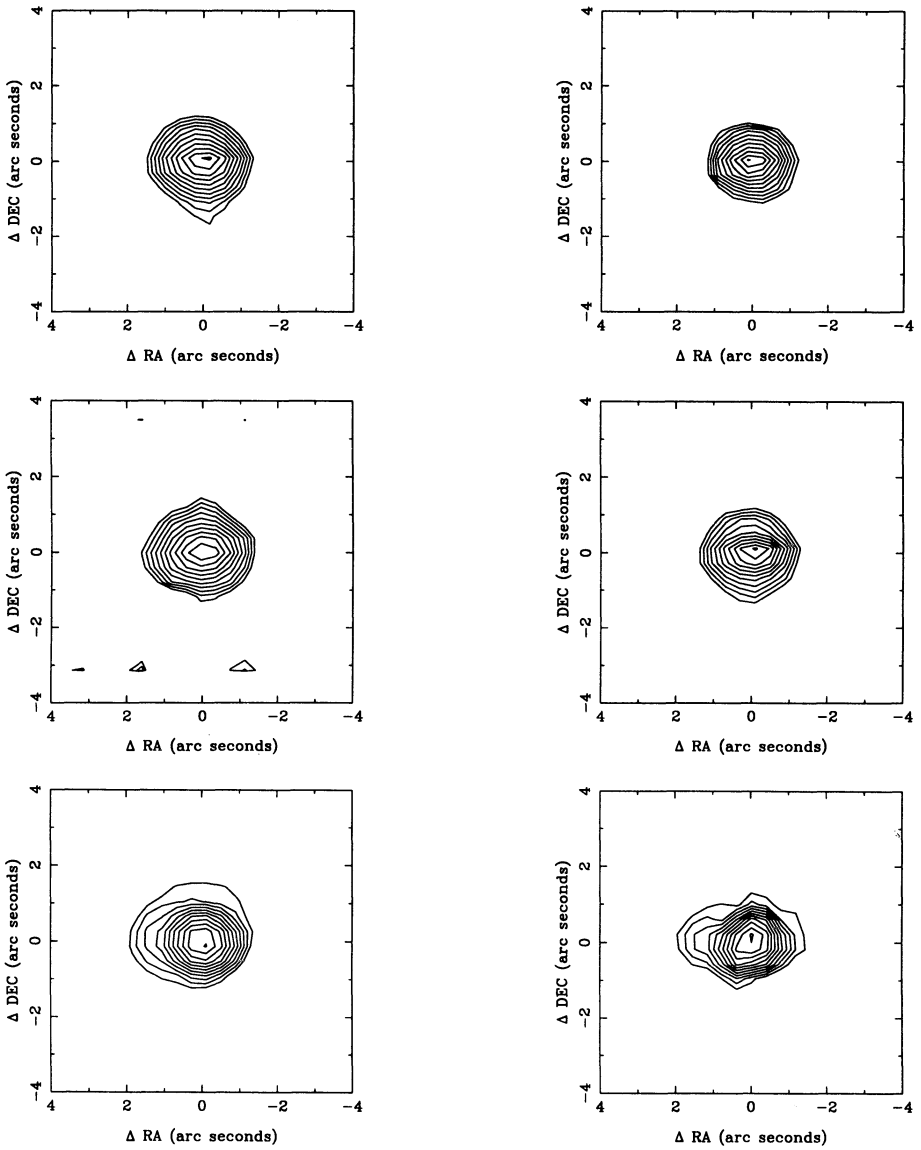

FIG. 2.—OH 26.5+0.6 (*left*) and γ Aql (*right*) at 8 μm (*top*), 10 μm (*middle*), and 12.5 μm (*bottom*). Contour levels in all images are evenly spaced on a $\log_{10}$ scale with contour interval = 0.13. Minimum contour levels (listed as left to right, top to bottom) are 7.7, 4.4, 0.53, 2.7, 4.0, and 1.4 Jy arcsec^2.

infrared to the radio. It is a luminous OH maser object. Herman & Habing (1985) monitored the OH emission of this object over several years and found a period of 1556 days. The OH flux varies by almost a factor of 3 during one cycle. Engels et al. (1983) observed this star in the near-infrared and found a similar period of 1630 days. The *K*-band flux varied by 3.86 mag between the maximum and minimum phases. A pulsation model with dust condensation for has been calculated for OH 26.5+0.6 by Suh, Jones, & Bowen (1990).

In this section, we will develop a self-consistent model in an attempt to explain both the infrared and submillimeter observations. The infrared data suggest a circumstellar shell which is extremely optically thick, while some CO data suggest significantly lower mass loss in the outer part of the envelope.

We will first model the observed infrared emission to derive the dust mass-loss rate in the superwind. Once we know this, we also know the momentum transfer to the gas ($\sim \tau L/c$), and it can then be used to derive the gas mass-loss rate from the observed gas outflow velocity ($\dot{M} \sim \tau L/cv_{\rm exp}$). Finally, the gas temperature distribution can be derived from the energy equation, where the heating is mainly caused by the viscous dust-gas interaction and the cooling is dominated by the expansion and molecular rotational line emission (Justtanont et al. 1994). For the outer shell, we will use the lower level CO observations to constrain the mass-loss rate. We will summarize the physics of a radiatively driven wind. The double shell structure of the circumstellar envelope of OH 26.5+0.6 is discussed, along with the infrared dust and CO emission. We have also calculated a number of other models for the CO emission.

3.1. *The Radiatively Driven Wind*

The equation of motion of the gas driven by radiation pressure on dust grains is given by (Tielens 1983)

$$v\frac{dv}{dr} = \frac{GM_*}{r^2}(\Gamma - 1)\,, \qquad (1)$$

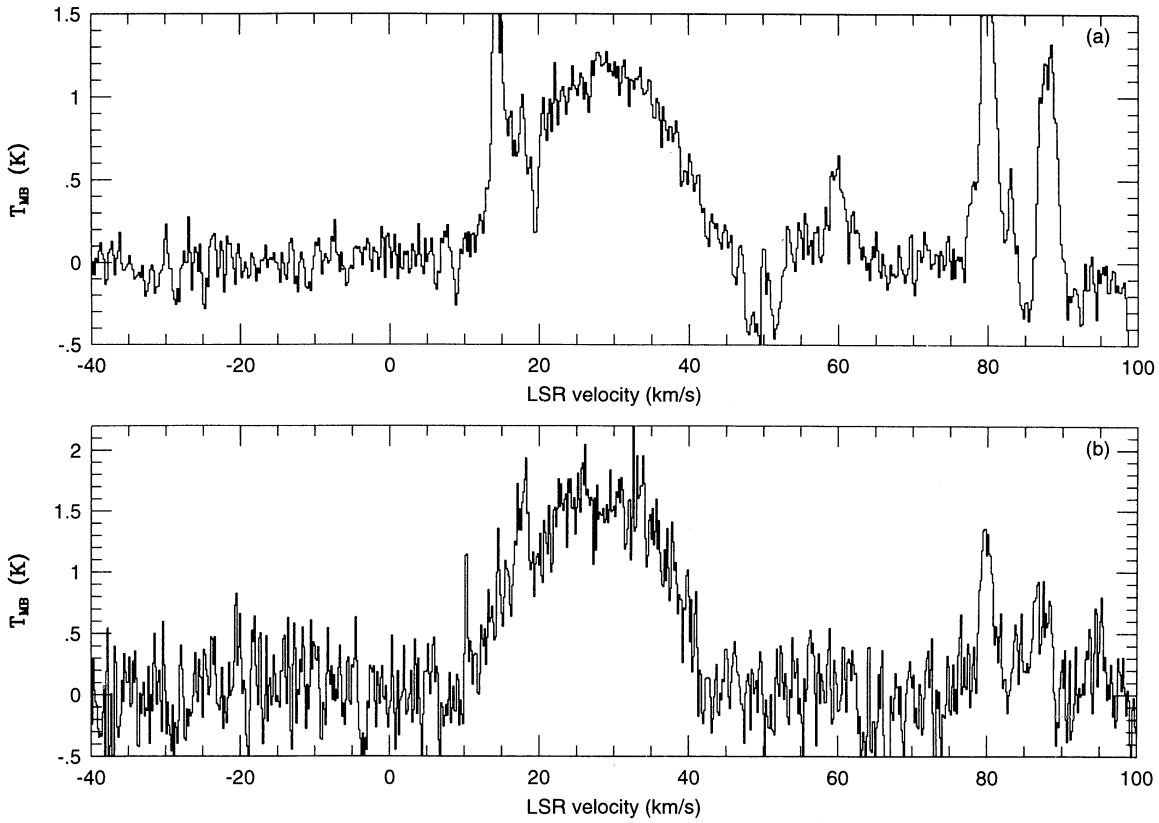

FIG. 3.—The observed CO $J = 3$–2 (*a*) and 4–3 (*b*) line profiles of OH 26.5+0.6 using the JCMT. Antenna temperatures have been corrected for the beam efficiencies.

where G is the gravitational constant, M_* is the stellar mass, and Γ is the ratio of the radiation pressure and the gravitational force. Taking the grain size distribution into account, Γ can be expressed as (See Justtanont et al. 1994)

$$\Gamma = \frac{3v}{16\pi\rho_s cGM_* \dot{M}} \iint \frac{Q(\lambda, a)\Gamma(\lambda)\dot{M}_d(a)}{a(v + v_{\rm drift})}\, d\lambda\, da\,, \qquad (2)$$

where $\dot{M}$ refers to the gas mass-loss rate, $\dot{M}_d(a)$ is the dust mass-loss rate for grains of size a, ρ_s is the dust specific density, $Q(\lambda, a)$ is the dust extinction coefficient, $L(\lambda)$ is the stellar luminosity, v is the gas velocity, and $v_{\rm drift}$ is the dust drift velocity relative to the gas. From these equations, the gas velocity can be calculated as a function of the radial distance from the star. We assume that the dust is formed at the condensation temperature of silicates ($\sim$1000 K). The dust radiative transfer calculation (§ 4) places the inner radius of the dust shell at 4.5×10^{14} cm. We also assume that at this point, the gas is traveling at the thermal sound speed ($\sim$3 km s^{-1} at 1000 K).

Assuming a stellar mass, and adopting a dust mass-loss rate and a dust condensation radius obtained from modeling the infrared energy distribution, we calculate the dust-to-gas mass ratio used to drive the outflow to the terminal velocity, observed from either CO or OH maser observations through an iterative process. Using mass conservation, this calculation will also result in the dust and gas density radial distribution.

The gas kinetic temperature, T, can be calculated by solving the energy balance (see Goldreich & Scoville 1976):

$$\frac{1}{T}\frac{dT}{dr} = \frac{-4}{3r}\left(1 + \frac{d\ln v}{2\,d\ln r}\right) + \frac{2(H-C)}{3vn_{\rm H}2kT(1+f)}\,, \qquad (3)$$

where H and C are the total heating and cooling rates, $n_{\rm H}$ is the atomic hydrogen density, and f is the ratio of the atomic to molecular hydrogen. The full detail of this calculation is presented by Justtanont et al. (1994).

3.2. *Mass-Loss History*

Figure 2 shows images of OH 26.5+0.6 at 8.5, 10, and 12.5 μm, along with the calibration star γ Aql (taken to be a point source at all three wavelengths). The contours are logarithmically spaced. OH 26.5+0.6 is unresolved at all wavelengths, indicating the compact nature of the dust-emitting region. After deconvolving these images, the full width at half-maximum is $\sim$0.″5. Since the object appears unresolved, this is the upper limit of the emitting region. For a source distance of 1.37 kpc, this corresponds to an upper limit to the size of the emitting region of $\sim 10^{16}$ cm. With the wind terminal velocity of 15.4 km s^{-1} (Bowers, Johnston, & Spencer 1983), the stars must have entered the superwind phase with a dramatically increased mass-loss rate within the past 200 years.

Heske et al. (1990) reported results of CO $J = 1$–0 and $J = 2$–1 lines, using the 30 m IRAM telescope. The 1–0 line was not detected, while the 2–1 line had a peak antenna temperature of 1.4 K. The low 1–0 antenna temperature implies a low mass-loss rate. Since each rotational line arises from a different region, it is reasonable to assume that mass loss has increased inward of the regions where the 2–1 and 1–0 lines originate.

From these data, we assume the structure of the envelope to be as follows: An inner region with a high gas mass-loss rate (5.5×10^{-4} $M_\odot$ yr^{-1}), the superwind, which extends out to

8×10^{15} cm. This is surrounded by an outer region, the AGB wind, in which the gas mass-loss rate falls to $10^{-6}\ M_\odot\ \mathrm{yr}^{-1}$, out to where CO is photodissociated ($\sim 6 \times 10^{16}$ cm; Mamon, Glassgold, & Huggins 1988). Extensive model calculations show that these values for the mass-loss rate and the radius of the superwind region provide the best fit to all the data.

4. THE INFRARED ENERGY DISTRIBUTION

This source has previously been modeled in the infrared by Bedijn (1987), Schutte & Tielens (1989), and Justtanont & Tielens (1992). The 10 μm spectrum shows a very deep absorption feature, indicating that the envelope is very optically thick.

The radiative transfer calculation is based on a numerical code developed by Haisch (1979) which uses a generalized two-stream Eddington approximation to solve for the emergent flux. It assumes spherical symmetry. An interstellar grain size distribution (Mathis, Rumpl, & Nordsieck 1977) is included. The dust optical constants used is model (a) from Justtanont & Tielens (1992) with the ratio of the 20:10 μm peak value of 0.8, which is appropriate for a star with a very thick circumstellar shell, since the ratio is empirically known to be dependent on the mass-loss rate (Bedijn 1987). The far-infrared extinction efficiency is assumed to fall as λ^{-1}. The main differences between our present model for the dust shell and our previous work are the dust density and the inclusion of the acceleration zone of the outflow where dust is formed. The structure, i.e., density, in this zone is calculated from the gas and dust interaction described in § 3.1 and the mass-loss scheme described in § 3.2. The input parameters are listed in Table 1. We assumed the distance to the source of 1.37 kpc, the average value derived from the phase lag technique by van Langevelde, van der Heiden, & van Schooneveld (1990).

TABLE 1

INPUT PARAMETERS FOR OH 26.5+0.6 (MODEL 1)

Parameter	Value
M_*	$8\ M_\odot$
$T_{\rm eff}$	2200 K
R_*	6.0×10^{13} cm
$R_{\rm in}$	4.5×10^{14} cm
$R_{\rm COphot}$	5.95×10^{16} cm
$\dot{M}_d$	$2 \times 10^{-6}\ M_\odot\ \mathrm{yr}^{-1}$ for $r < 8 \times 10^{15}$ cm, $3.6 \times 10^{-9}\ M_\odot\ \mathrm{yr}^{-1}$ for $r > 8 \times 10^{15}$ cm
$\dot{M}_d/\dot{M}_g$	3.6×10^{-3}
$v_{\rm exp}$	15.4 km s^{-1}
D	1.37 kpc
$f_{\rm CO}$	3×10^{-4}

The calculated dust mass-loss rate is $2 \times 10^{-6}\ M_\odot\ \mathrm{yr}^{-1}$, giving a dust density at the inner radius of 2.4 cm^{-3}. The dust mass-loss rate beyond the radius of 8×10^{15} cm is taken to be $3.6 \times 10^{-9}\ M_\odot\ \mathrm{yr}^{-1}$. The resulting infrared energy distribution is compared to published photometry from Evans & Beckwith (1977), Werner et al. (1980), *IRAS* broadband photometry, and the spectrum taken at 10 and 20 μm, using CGS3 (Fig. 4). The *IRAS* photometry at 100 μm is higher than

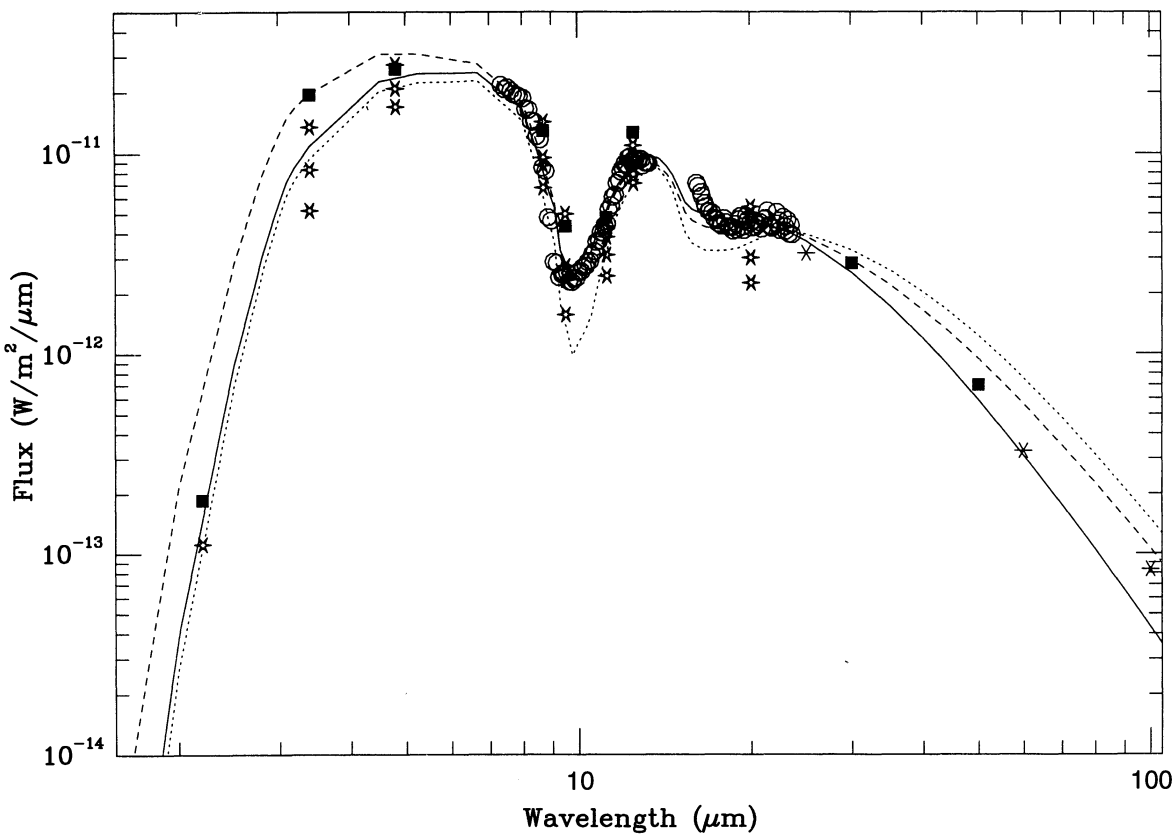

FIG. 4.—IR energy distribution of OH 26.5+0.6. Solid line is a model with dust mass-loss rate of $2 \times 10^{-6}/3.6 \times 10^{-9}\ M_\odot\ \mathrm{yr}^{-1}$ with the discontinuity of density at 8×10^{15} cm (model 1); dotted line is a model with a constant dust mass-loss rate of $2 \times 10^{-6}\ M_\odot\ \mathrm{yr}^{-1}$; dashed line is a model with a constant dust mass-loss rate of $1.2 \times 10^{-6}\ M_\odot\ \mathrm{yr}^{-1}$. Both models with a constant dust mass-loss rate overestimate the flux beyond 25 μm, implying there is too much cold dust. *Open circles*: CGS3 data; *asterisks*: *IRAS* broadband flux; *squares*: Werner et al. (1980); *stars*: Evans & Beckwith (1977).

expected. This may reflect confusion at this wavelength, since the source is in the galactic plane (*IRAS* Point Source Catalog). We have decided not to separate observations according to pulsational phase but rather to fit the overall shape. From the available photometry, OH 26.5+0.6 varies by as much as 35% over a period of 2 years in the near- to mid-infrared (Evans & Beckwith 1977; Fig. 4). Also, Forrest et al. (1978) reported a change of the 10 μm depth with time, decreasing in depth with increasing infrared flux. In view of this, it is difficult to fit all the data taken at different epochs with one model. Our model represents the best overal fit to the available data (solid line in Fig. 4). Most of this optical depth is associated with the dust in the superwind. The calculated infrared luminosity is $1.4 \times 10^4\ L_\odot$, consistent with what is expected from an OH/IR star. Although there are available data at the submillimeter wavelength, e.g., Walmsley et al. (1991) and van der Veen et al. (1995), we have chosen not to extend our model fit to those data because of conflicting observations and because the dust opacity at such a long wavelength is not well known. We have also calculated an alternative model which has a constant dust mass-loss rate throughout the envelope. In order to fit both photometry and spectroscopy data, the dust mass-loss rate has to be reduced to $1.2 \times 10^{-6}\ M_\odot\ \mathrm{yr}^{-1}$ (dashed line in Fig. 4), with a slightly hotter star (2300 K rather than 2200 K for the superwind-AGB mass-loss model) in order to get the dust column density required at 10 μm. Note that if the dust mass-loss rate remains at $2 \times 10^{-6}\ M_\odot\ \mathrm{yr}^{-1}$ throughout the envelope, the depth of the 9.7 μm feature is much deeper than observed (dotted line in Fig. 4). The superwind-AGB mass-loss model fits photometry points better in both the near- and, especially, far-infrared, but in view of the variability of OH 26.5+0.6, it is difficult to distinguish from the spectral energy distribution alone which model better describes the data.

We calculated intensity profiles for three different wavelengths, 8.5, 9.7, and 12.5 μm, in order to compare them to our mid-infrared results and a published visibility function of the 8.7 and 9.7 μm speckle observations of OH 26.5+0.6 by Fix & Cobb (1988), who resolved the circumstellar envelope at 9.7 μm. The calculated FWHM of the intensity at 8.5 and 12.5 μm of 0.″12 and 0.″16, respectively (Fig. 5) are considerably smaller than the observed upper limit obtained from the mid-infrared images. The FWHM at 9.7 μm, as expected, is slightly larger, i.e., 0.″22. We have calculated the visibility function $V(f)$ from the intensity using

$$V(f) = \int_0^{\theta_{\max}} I_\nu(\theta) J_0(2\pi f\theta)\theta\, d\theta\ , \qquad (4)$$

where f is the frequency in cycles per arcsec and, $\theta = p/D$, p is the impact parameter, D is the distance, and J_0 is the Bessel function of the zeroth order. Our model results are compared to the published data in Figure 6. Our calculated visibility curve matches the data at 9.7 μm well for the superwind-AGB mass-loss model as well as for the best-fit, constant mass-loss model ($\dot{M}_d = 1.2 \times 10^{-6}\ M_\odot\ \mathrm{yr}^{-1}$). There is a slight discrepancy between calculated and observed visibility curves at 8.7 μm. However, both observations and models suggest that OH 26.5+0.6 is on the verge of being resolved at 8.7 μm. Again, both models give similar fits to the visibility data. We conclude

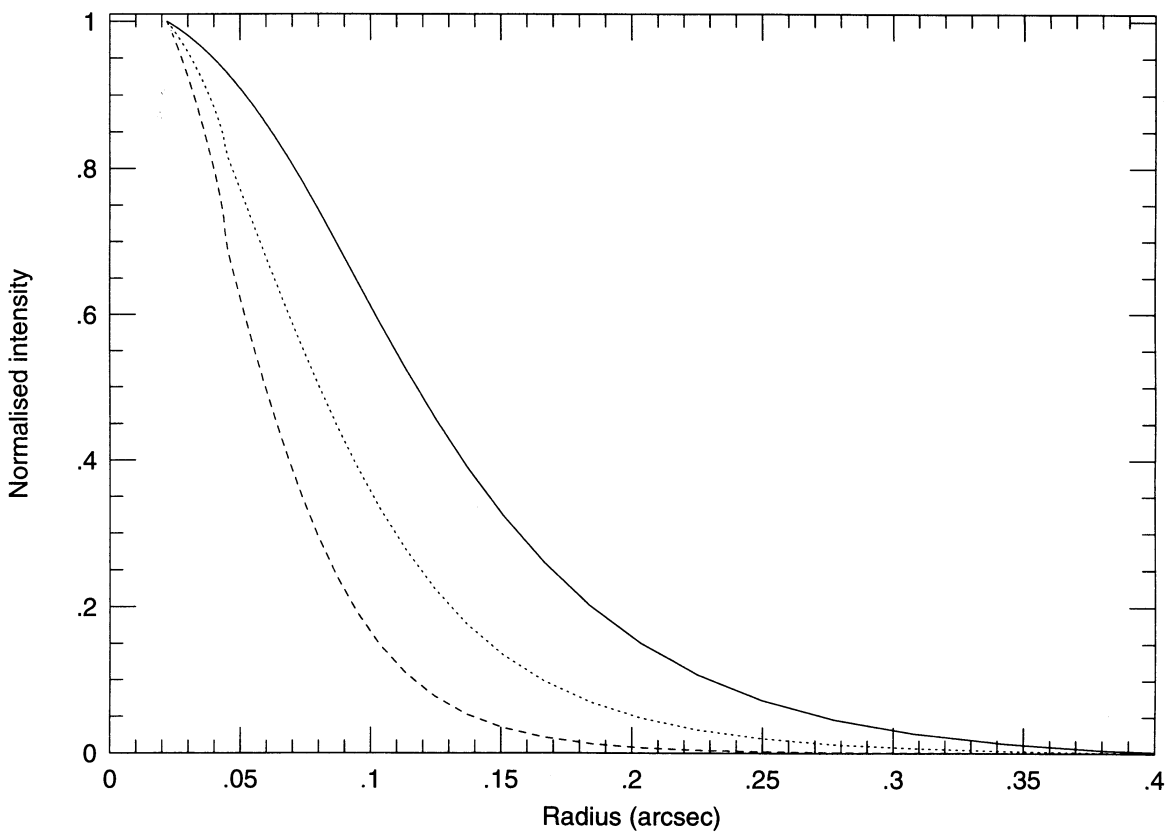

FIG. 5.—Calculated infrared intensity profile at 8.5 (*dashed line*), 9.7 (*solid line*), and 12.5 μm (*dotted line*) as a function of radius

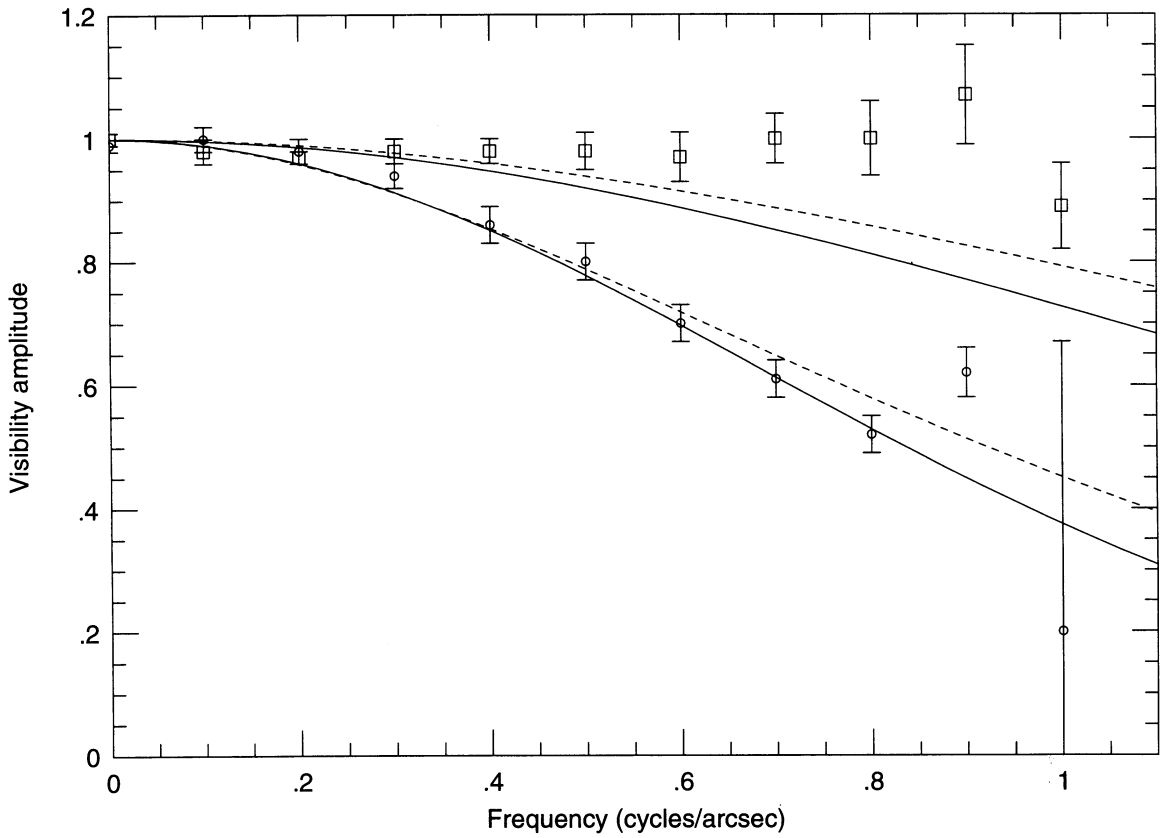

FIG. 6.—Comparisons of calculated visibility functions of model 1 (*solid line*) and model 7 (*dashed line*) with the data taken from Fix & Cobb (1988). *Circles*: 9.7 μm; *squares*: 8.7 μm.

from the infrared modeling that the present mass-loss rate is very high and that the infrared emission is not sensitive to the mass-loss rate longer than 200 years ago.

5. THE CO LINE EMISSION

The radiative transfer in molecular lines is calculated using a Newton-Raphson method developed by Schönberg & Hempe (1986). The calculation does not assume the Sobolev approximation. It has been demonstrated that the Sobolev approximation breaks down in red giants, since the stochastic velocity is a significant fraction of the local outflow velocity (Schönberg 1985; Justtanont et al. 1994). Once the level populations have been determined, the line profile for each transition can be calculated using the formal radiative transfer integral (Schönberg 1988).

In calculating the radiative transfer, two input parameters which have major influence on the calculated antenna temperature are the gas density and kinetic temperature distributions. By varying either distribution, the same effect can be achieved in the level population of a rotational state. It is difficult to disentangle these two distributions when calculating antenna temperatures for low mass-loss rates ($< 10^{-5}$ $M_\odot$ yr^{-1}). For very high mass-loss rates when the envelope is optically thick in the CO lines, keeping the gas temperature the same while increasing the mass-loss rate has little effect on the peak antenna temperature because of subtle optical depth effects, but it will make the line profile narrower and sharper. On the other hand, the peak antenna temperature is very sensitive to the assumed gas temperature distribution (see § 5.2). Hence, in the case of OH 26.5+0.6, the higher CO lines (J = 3–2, 4–3, etc.), which probe the superwind region, can be used to constrain the temperature structure of the envelope. For the lower CO lines (J = 1–0 and 2–1), which originate in the outer tenuous envelope, both the density and temperature affect the observed antenna temperatures. Hence, for OH 26.5+0.6, observed antenna temperatures at various rotational transitions allow us to investigate the gas kinetic temperature in the envelope while the mass-loss rate has been determined from infrared energy distribution, infrared imaging, and CO line profiles.

In order to solve for the line emission, the gas density and kinetic temperature structures of the envelope are required. Assuming a stellar mass of 8 $M_\odot$, and using the derived dust mass-loss rate of 2×10^{-6} $M_\odot$ yr^{-1} starting at the inner radius of 4.5×10^{14} cm, the momentum equation (eq. [1]) implies that a dust-to-gas mass ratio of 3.6×10^{-3} is required to drive the wind to the observed terminal velocity of 15.4 km s^{-1}. This translates to a gas mass-loss rate of 5.5×10^{-4} $M_\odot$ yr^{-1} in the inner part. For the outer AGB wind, the low-level CO observations require a gas mass-loss rate of 10^{-6} $M_\odot$ yr^{-1}. We assume that there is no velocity difference between the superwind and the AGB wind, e.g., OH and CO observations give an outflow velocity of $\sim$15 km s^{-1}. Hence, in this model, there is little interaction between the superwind and the AGB wind. The weak dependence of the outflow velocity on the mass-loss rate is a common characteristic for O-rich AGB envelopes for $\dot{M} > 10^{-6}$ $M_\odot$ yr^{-1}. For C-rich objects, the

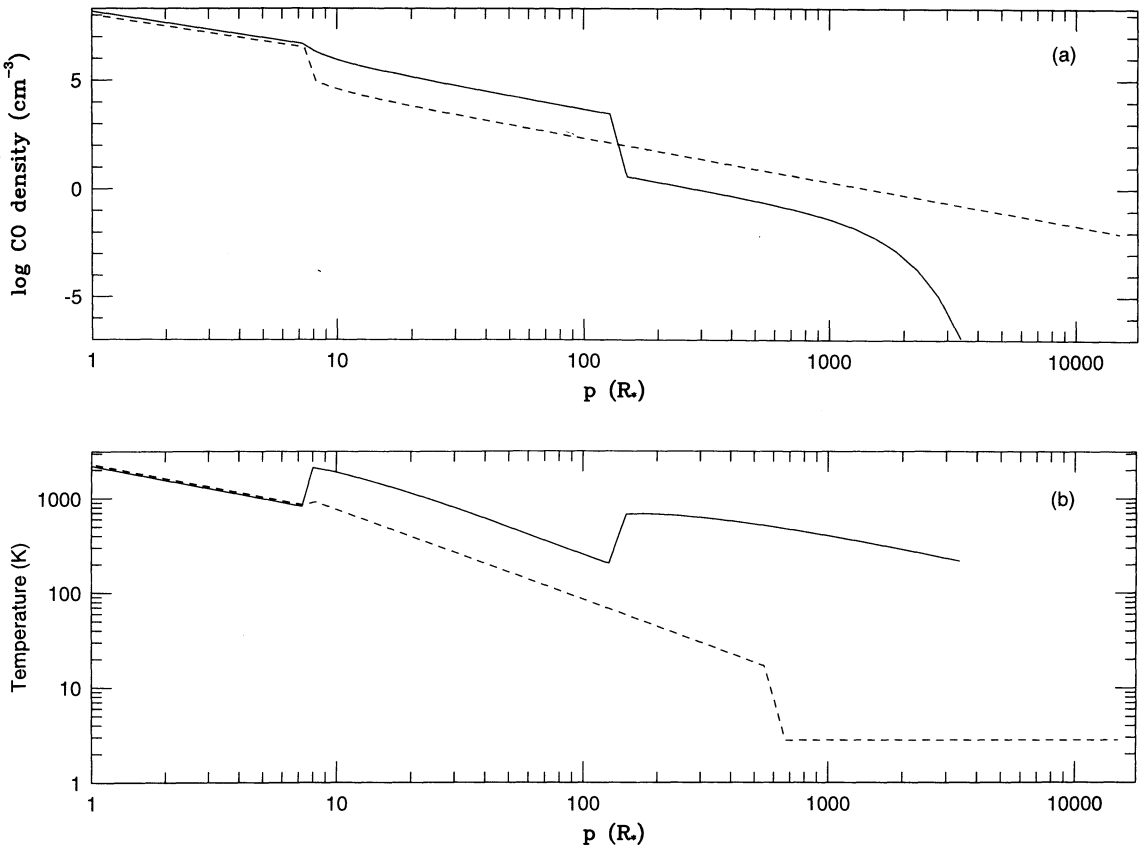

FIG. 7.—(*a*) Density and (*b*) temperature structures of the envelope for model 1 (*solid line*) and model 7 (*dashed line*). Note that because model 7 has a constant gas mass-loss rate of $3.9 \times 10^{-4}\ M_\odot\ \mathrm{yr}^{-1}$, the outer radius of the envelope is much larger than model 1, which has a gas mass-loss rate of $10^{-6}\ M_\odot\ \mathrm{yr}^{-1}$ owing to photodissociation of CO.

expected velocity differences are larger (Habing, Tignon, & Tielens 1994).

The calculated CO density profile is shown in Figure 7*a*. The derived gas kinetic temperature distribution is then a combination of the two mass-loss regimes. The inner part ($r \leq 8 \times 10^{15}$ cm) is driven by the dust mass-loss rate of $2 \times 10^{-6}\ M_\odot\ \mathrm{yr}^{-1}$. There is a jump in the temperature at the dust condensation radius (Fig. 7*b*, *solid line*), signifying the sudden onset of the contribution by the viscous heating. Another break in the temperature profile occurs at the interface of the high and low mass-loss shells. The gas temperature is considerably higher in the outer part owing to the fact that for a low mass-loss rate, the density of H_2O (the major coolant) is very much lower and the photodissociation radius of H_2O is very small, compared to a high mass-loss region. The dust-gas drift velocity for the outer part is also much higher, since the gas density is too low for all dust grains to transfer their momentum in collisions ($v_{\mathrm{drift}} \propto \dot{M}^{-0.5}$). This effectively means the heating rate is high, since it is proportional to $\dot{M} v_{\mathrm{drift}}^3$, i.e., the heating rate per H-atom scales with $\dot{M}^{-0.5}$ (Justtanont et al. 1994).

We have calculated a variety of models. Parameters of the models discussed in this paper are listed in Table 2. Calculated antenna temperatures and integrated intensities for a 15 m telescope, working at its diffraction limit for each transition, are presented in Table 3.

5.1. *The Standard Model*

The line strength increases with J as we probe into the superwind region (model 1 in Table 3). The regions in which the different CO rotational transitions originate are shown in Figure 8*a*. For the $J = 1$–0 and $J = 2$–1 lines, the majority of the line intensity originates in the AGB wind, beyond the superwind region, while for the $J = 3$–2 and higher transitions, most of the emission comes from the very dense region. Owing to the change in density at $r = 8 \times 10^{15}$ cm, the calculated line

TABLE 2

GAS MASS-LOSS RATES AND GAS KINETIC TEMPERATURES FOR VARIOUS CO MODELS

Model	$\dot{M}$ ($M_\odot$ yr^{-1})	Temperature Distribution
1.....	$5.5 \times 10^{-4}/10^{-6}$ [a]	from eq. (4)
2.....	$5.5 \times 10^{-4}/10^{-6}$ [a]	T from model 1 divided by 3
3.....	$1.8 \times 10^{-4}/10^{-6}$ [a]	same as model 1
4.....	5.5×10^{-4} constant	from eq. (4)
5.....	10^{-6} constant	from eq (4)
6.....	5×10^{-5} constant	from eq. (4)
7.....	3.9×10^{-4} constant	$1000(r/r_i)^{-0.95}$ for $r < 4 \times 10^{16}$ cm; 2.8 K for $r > 4 \times 10^{16}$ cm

NOTE.—The best fit is model 1 with superwind-AGB mass loss model. Model 7 is the best fit for a constant density regime.

[a] Two-shell model. First number is the value of $\dot{M}$ in the inner part, and 10^{-6} is the value of $\dot{M}$ in the outer part.

TABLE 3

CO EMISSION[a]

	$J = 1$–0		$J = 2$–1		$J = 3$–2		$J = 4$–3		$J = 5$–4		$J = 6$–5	
MODEL	T	I	T	I	T	I	T	I	T	I	T	I
Observations.....	<0.1	...	0.5[b]	7.8[b]	1.2	25.8	1.6	36.0	...	...	...	...
Model 1	0.07	1.6	0.4	10.2	1.4	27.9	2.0	41.2	3.0	60.6	4.1	83.3
Model 2	0.04	1.0	0.5	8.9	0.5	11.2	0.7	15.4	1.0	20.7	1.3	26.9
Model 3	0.03	1.0	0.3	8.4	1.1	24.3	1.9	39.1	2.9	58.6	4.0	81.4
Model 4	8.40	197.2	17.9	424.6	23.5	553.5	28.1	654.1	31.8	732.1	34.8	793.0
Model 5	0.01	0.3	0.1	3.0	0.2	5.4	0.4	8.6	0.3	8.4	0.4	9.6
Model 6	0.21	5.7	0.5	13.2	0.6	15.2	0.7	17.4	0.8	19.0	0.9	20.8
Model 7	0.08	1.8	0.5	10.3	1.1	22.3	1.6	33.4	1.9	40.2	2.1	43.9

[a] The observed and calculated peak antenna temperatures, T (K), and line strengths, I (K km s^{-1}), for each transition for all models in Table 2 for a 15 m telescope working at the diffraction limit for each transition.

[b] The scaled antenna temperature and line intensity from IRAM telescope to a 15 m telescope.

profiles are neither smooth nor symmetric around the stellar velocity (Fig. 9, *solid line*). There is more emission from the blue side of profile, since the receding back of the shell is partly obscured by the superwind.

The line shapes, indicative of the gas mass-loss rate, fit the observed data reasonably well. The $J = 3$–2 profile, unfortunately, suffers from interstellar contamination (around 15 km s^{-1}), since OH 26.5+0.6 is in the galactic plane. The calculated antenna temperatures for both $J = 3$–2 and 4–3 lines are within the uncertainty limit of the observations ($\sim$20%). Both lines originate from the superwind region where density is high. The model overestimates the temperature for the $J = 2$–1 line observed by IRAM (Heske et al. 1990); however, the calculated temperature is within the uncertainty quoted for the observed value. The observed line profile seems narrower than the calculated one at the red side. The 2–1 observation was approximately corrected for interstellar emission by subtraction of the emission observed at nearby positions. Possibly, the disagreement between our model and the observed 2–1 profile (or between the 2–1 and the 3–2 and 4–3 profiles) at these velocities reflects an overestimated correction factor for interstellar 2–1 emission.

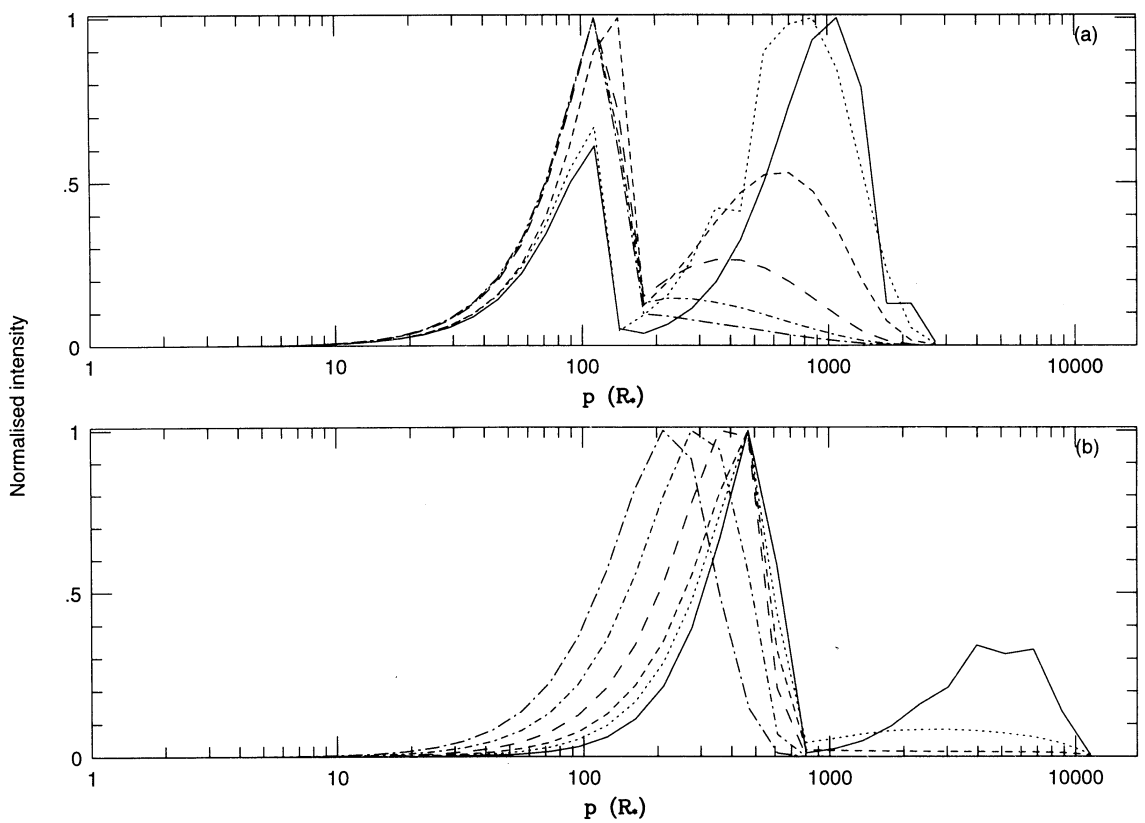

FIG. 8.—Distribution of line intensity $[p^3 I(p)]$ as a function of the impact parameter, p, shows where the emission of each line originates for (*a*) model 1 and (*b*) model 7. *Solid line*: $J = 1$–0; *dotted line*: $J = 2$–1; *short-dashed line*: $J = 3$–2; *long-dashed line*: $J = 4$–3; *dot–short-dashed line*: $J = 5$–4; *dot–long-dashed line*: $J = 6$–5.

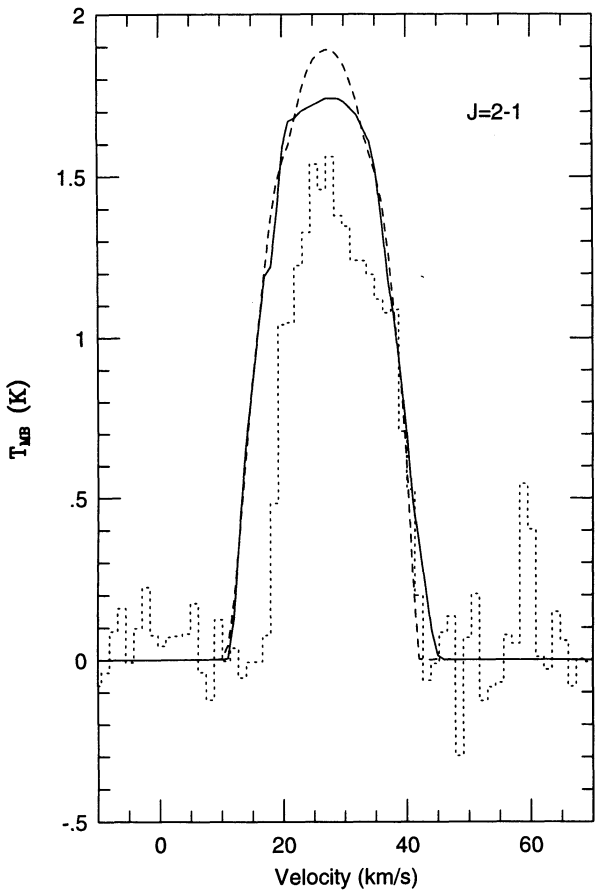

FIG. 9a

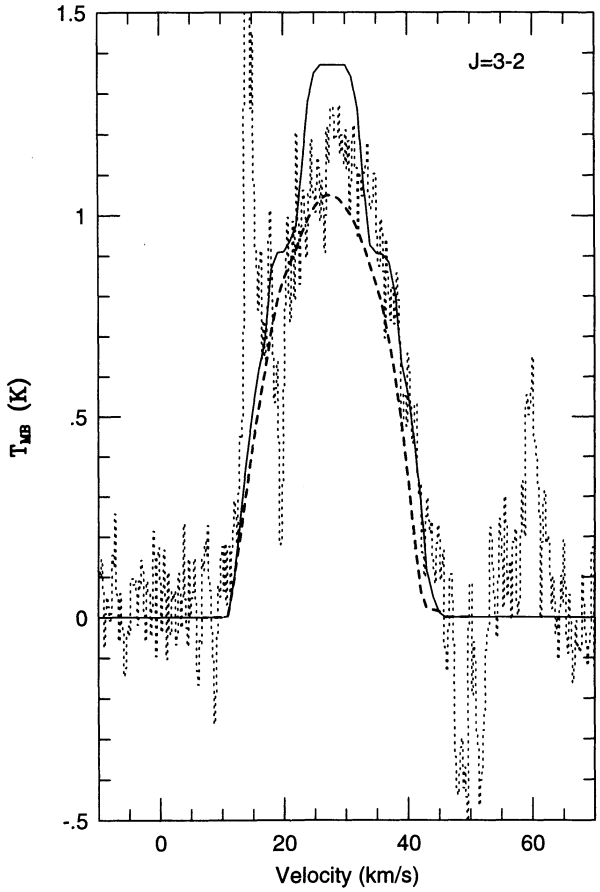

FIG. 9b

FIG. 9.—Comparisons of observed CO lines with observations. Solid line is from model 1, and dashed line is from model 7. (*a*) $J = 2$–1 IRAM data taken from Heske et al. (1990); (*b*) $J = 3$–2 from JCMT; (*c*) $J = 4$–3 from JCMT.

5.2. *Variations on the Standard Model*

To demonstrate the effects of the mass-loss rate and temperature, we calculated a number of other models. Their parameters are summarized in Table 2. Model 2 has an identical density profile to the standard model (model 1), but the gas kinetic temperature has arbitrarily been reduced by a factor of 3. Model 3 has the same gas kinetic temperature as model 1, but the density has been reduced by a factor of 3. Since we want to illustrate that for a very optically thick case, the calculated antenna temperatures are independent of the density structure in the envelope, we only change the gas mass-loss rate in the superwind region. In the outer envelope, we keep the same gas mass-loss rate of $10^{-6}\ M_\odot\ \mathrm{yr}^{-1}$. We also include two models with a constant gas mass-loss rate of 5.5×10^{-4} and $10^{-6}\ M_\odot\ \mathrm{yr}^{-1}$ (models 4 and 5) which are the superwind and AGB wind gas mass-loss rates used in the standard model. Model 6 has a gas mass-loss rate of $5 \times 10^{-5}\ M_\odot\ \mathrm{yr}^{-1}$, which results from using the CO $J = 2$–1 antenna temperature observed by Heske et al. (1990) to estimate the gas mass-loss rate (Knapp & Morris 1985). Finally, for model 7, we adopt a constant mass-loss rate of $3.9 \times 10^{-4}\ M_\odot\ \mathrm{yr}^{-1}$, which resulted from a dust mass-loss rate of $1.2 \times 10^{-6}\ M_\odot\ \mathrm{yr}^{-1}$ being driven radiatively (see §§ 3.1 and 4), and adjusted the gas kinetic temperature law until a reasonable agreement with the observations was obtained.

As can be seen in Table 3, reducing the gas temperature (model 2) results in much lower calculated antenna temperatures compared to the standard model. In contrast, the density (model 3) has little effect. Also, none of the simple models (models 4, 5, and 6) with r^{-2} density and gas temperatures derived from equation (4) would be able to account for all the observed CO lines.

We were able to fit the observed CO data using a constant gas mass-loss rate by assuming a very steep temperature law of the form $(r/r_i)^{-0.95}$ and arbitrarily fix the gas temperature to 2.8 K for $r > 4 \times 10^{16}$ cm (model 7). The calculated line profiles are shown in Figure 9 (*dashed line*). This model is in reasonable agreement with the 2–1, 3–2, and 4–3 observations. Table 4 lists, for models 1 and 7, the physical conditions of the region in which the peak emission of each line originates. As can be seen, conditions for each line in both models are very different. Presently, it is difficult to distinguish between these two models based on only CO data up to $J = 4$–3. Observations of higher rotational transitions such as $J = 6$–5 should be able to confirm one way or the other, since model 7 has an antenna temperature lower by a factor of 2 compared to model 1, reflecting the lower gas temperature in the emitting zones. We favor model 1 because it provides an overall better fit to all data (infrared and CO). Also, there is no physical reason why the gas temperature should remain 2.8 K for the outer half for the constant mass-loss rate model (model 7).

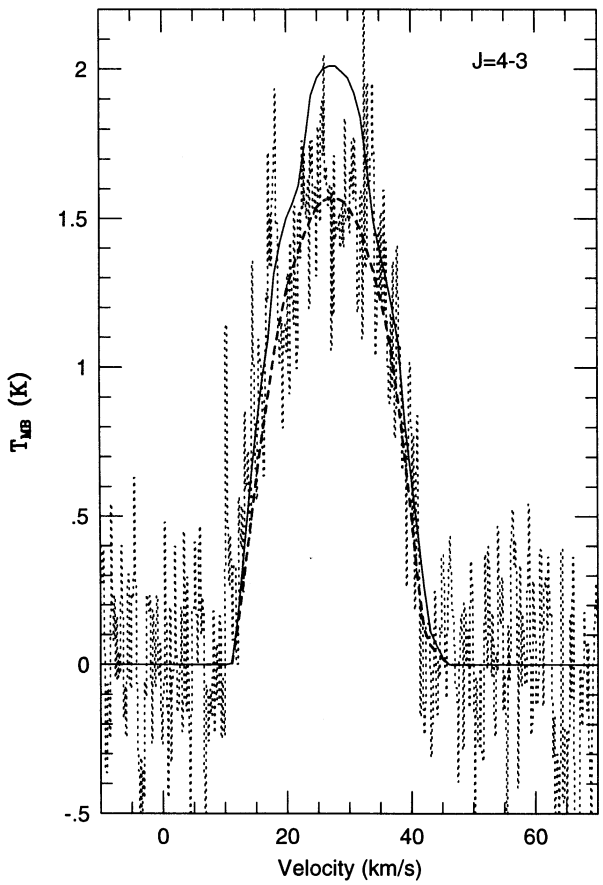

FIG. 9c

5.3. *The AGB—Superwind Transition*

It is of considerable interest to determine how rapid (or smooth) the transition from the AGB wind to the superwind gas. We have therefore calculated another variant of model 1 which has a region in which the mass-loss rate drops off slowly, rather than discontinuously. We take the radius of the superwind to be the same (8×10^{15} cm, which has been fixed by fitting the visibility function at 9.7 μm) and then have the gas mass-loss rate drop to $10^{-6}\ M_\odot\ \mathrm{yr}^{-1}$ linearly. From these studies, we conclude that the gas mass-loss rate should reach this $10^{-6}\ M_\odot\ \mathrm{yr}^{-1}$ limit at $r < 1.5 \times 10^{16}$ cm, otherwise the calculated emission lines of CO overestimate the observed values. This indicates that the change in mass-loss rate is a very abrupt ($\Delta t < 150$ yr) process in OH 26.5+0.6. Since the superwind started $\sim$200 yr ago in this object, the total mass lost by the star in the superwind so far is $\sim 0.1\ M_\odot$.

There is a difference between the infrared source size and that estimated from the OH maser map. The VLA maps of this source by Herman et al. (1985) and Bowers & Johnston (1990) show that the OH emission originates in a shell at 2″–3″ (=4–6 $\times 10^{16}$ cm at 1.37 kpc), i.e., in the AGB wind. This suggests that there is significant mass loss farther out from the superwind region. The gas mass-loss rate estimated from the OH flux, using the expression from Baud & Habing (1983), is $4 \times 10^{-5}\ M_\odot\ \mathrm{yr}^{-1}$, which is much larger than that allowed by the CO observations at this radius. One of the assumptions in calculating mass-loss rates from OH maser luminosities is that masers are saturated. This requires the minimum column density for OH of $10^{17}\ \mathrm{cm}^{-2}$, i.e., $\dot{M}\ (M_\odot\ \mathrm{yr}^{-1})/v^2\ (\mathrm{km\ s}^{-1}) \geq 10^{-6}$ (Netzer & Knapp 1987). Clearly, this condition is not satisfied in the AGB wind; hence, the estimated mass-loss rate from OH maser luminosity is no longer reliable.

In radiatively driven wind models, the only unknown parameter in the dynamics which cannot be calculated from the fitting of the infrared energy distribution or the infrared imaging is the stellar mass. The masses of stars which evolve onto the AGB range from 1 to 8 $\dot{M}$. A star with a lower mass has a smaller gravitational attraction. Hence, a given dust mass-loss rate (from the infrared) can drive more gas to the same (observed) terminal velocity from a low-mass star than from a higher mass star. We have calculated antenna temperatures for a case of a low-mass ($1.5\ M_\odot$; $\dot{M} = 9.3 \times 10^{-4}\ M_\odot\ \mathrm{yr}^{-1}$) and a high-mass ($8\ M_\odot$; $\dot{M} = 5.5 \times 10^{-4}\ M_\odot\ \mathrm{yr}^{-1}$) star. The calculated antenna temperatures are very similar in both cases. This is due to the fact that their temperature structures calculated from the energy balance equation are almost identical. For stars with high gas mass-loss rates, the dominant cooling in the inner envelope is through the H_2 vibrational de-excitation. However, for density above the critical density, this cooling does not depend on the density. In the mid and outer part of the envelope, the main cooling process is just the adiabatic expansion, which is also independent of the mass-loss rate. As stated earlier, for high mass-loss rates, the antenna temperature is much more sensitive to the gas temperature than to the density.

In our calculation, we have adopted a stellar mass in the higher end (i.e., $8\ M_\odot$), and the star has to continue to lose mass at the present rate for another 1.3×10^4 yr before the core mass is reduced to $0.6\ M_\odot$, the optimum observed mass of white dwarfs in our Galaxy (Weidemann & Koester 1983). In contrast, for a $1.5\ M_\odot$ star, the present superwind phase need only last up to 900 yr. In any case, the 200 yr since the onset of the superwind in OH 26.5+0.6 is only a small fraction of the

TABLE 4

COMPARISON OF CALCULATED ANTENNA TEMPERATURES FOR MODELS 1 AND 7[a]

	Model 1				Model 7			
Transition	T_{MB} (K)	Radius (R_*)	T_g (K)	ρ_{CO} (cm^{-3})	T_{MB} (K)	Radius (R_*)	T_g (K)	ρ_{CO} (cm^{-3})
1–0	0.065	1092	400	0.03	0.083	471	20	9.7
2–1	0.44	870	420	0.06	0.49	471	20	9.7
3–2	1.37	141	450	31.6	1.05	471	20	9.7
4–3	2.01	112	220	3500	1.57	361	25	16
5–4	2.95	112	220	3500	1.89	276	32	28
6–5	4.09	112	220	3500	2.07	211	42	48

[a] Listed are the radius at which the peak emission of each transition occurs and the temperature and density at that point.

total duration of this phase. Hence, it seems rather fortuitous that we caught OH 26.5+0.6 at the start of the superwind. Yet, the characteristics of this recent onset of the superwind, a heavily obscured AGB star with low CO $J = 1$–0 emission, seems to be common for many extreme OH/IR stars (Heske et al. 1990). This seems to point toward a punctuated superwind evolution, in which periods of heavy mass loss are interspersed in much longer periods of lower mass loss, possibly regulated by helium shell flashes (e.g., Vassiliadis & Wood 1993). Evidence for this can be found in CO observations of a few C stars (Olofsson et al. 1993) and the post-AGB object, GL 2688, whose image at I shows concentric rings around the central object (Crabtree & Rogers 1993; Latter et al. 1993). The interpretation for these rings is a series of interrupted mass loss just before the star evolved off the AGB. The timescale for each mass-loss phase is $\sim$750 yr (Skinner et al. 1995).

The idea of a star terminating its AGB life with a superwind has been calculated by Bowen & Willson (1991). Their calculations show that all stars will undergo the superwind phase as a result of an increase in the scale height and density at the condensation radius as the star evolves toward the tip of the AGB. However, this transition occurs much more slowly (2×10^4 yr) than the observations indicate. Vassiliadis & Wood (1993) have calculated the effects of thermal pulses on mass-loss rates and suggest that a star may undergo many superwind phases and that more massive stars will stay longer in the superwind phase than lower mass stars. Again, the transition timescale is rather long (2×10^4 yr). This is a general result for any models that are ultimately driven by changes in, say, mass wrought by the mass-loss process itself. In contrast, the observed transition timescale of $\leq 10^2$ yr indicates perhaps a Kelvin-Helmholtz timescale associated with the thermal pulses itself. So, if each thermal pulse lasts 500 years and loses $\sim 0.25\ M_\odot$, about 30 pulses are required to bring the stellar mass down to a typical white dwarf mass.

6. CONCLUSION

The kinematic, temperature, and density structures of circumstellar dust shells around late-type stars are closely coupled. Once dust is formed in the envelope, it is the major mechanism in driving the gas outflow. In doing so, it also heats the gas. The envelope cools adiabatically and radiatively via molecular rotational and/or vibrational lines. This, together with the gas density, determines the expected emission of the observed CO rotational lines. It is desirable then to understand the temperature structure of the gas as a function of radius in order to predict various line emission. Similar approaches to modeling the dust and gas emission around late-type stars have been conducted by, e.g., Sahai (1990), Kastner (1992), and Groenewegen (1994).

For OH 26.5+0.6, we have information on rotational lines of CO which sample different regions of the envelope. The lack of $J = 1$–0 emission suggests that the density in its emission zone is very low. Emission in higher rotational lines shows, however, the presence of denser and warmer gas. This leads quite naturally to a model with variable mass-loss rate. We have modeled the infrared energy distribution and calculated the dust mass-loss rate to be $2 \times 10^{-6}\ M_\odot\ \mathrm{yr}^{-1}$, which is very high, suggesting the star is in the final stage of the AGB. The size of this high-density zone is on the order of 8×10^{15} cm in radius in order to fit the speckle observations at 9.7 μm. Using this derived dust mass-loss rate, the gas mass-loss rate can be calculated directly from the momentum equations. The calculated gas mass-loss rate depends on the stellar mass. In general, we found $\dot{M} = 1.05 \times 10^3\ M_*^{0.3}$. For these high mass-loss rates, the momentum flux in the gas ($\dot{M}v$) has to equal the momentum flux in the dust ($\tau L/c$; see Cherchneff & Tielens 1994, Habing et al. 1994). For lower mass-loss rates, the drift velocity of the dust has to be taken into account.

For a source with a high mass-loss rate such as OH 26.5+0.6, the CO antenna temperature is no longer dependent on its density. It is now a strong function of the temperature structure of the envelope. Hence, lines of higher transitions ($J \geq 3$), which probe gas in the dense superwind, will depend mainly on the gas temperature. We have solved for the gas kinetic temperature using an energy balance equation which takes into account the gas heating by collisions with dust grains and adiabatic and radiative cooling. The calculated antenna temperatures for the CO $J = 2$–1, 3–2, and 4–3 transitions are in good agreement with the observations. In order to investigate the gas temperature of the envelope closer in toward the star, we need to observe higher rotational transition lines. We have been allocated time on the *Infrared Space Observatory* (*ISO*) for this purpose.

We have also calculated an alternative model with a constant mass-loss rate. Note that in this model, the required gas mass-loss rate is also very large ($3.9 \times 10^{-4}\ M_\odot\ \mathrm{yr}^{-1}$). In order to fit all the observed CO lines, the assumed gas temperature has to drop very steeply from the inner radius ($T \propto r^{-0.95}$) out to $r \sim 4 \times 10^{16}$ cm and has to remain 2.8 K beyond that radius. This rather ad hoc temperature distribution does not have a sound foundation in the physics of circumstellar shells. Moreover, the observed infrared dust continuum is somewhat better fitted by the superwind–AGB wind model discussed above, particularly in the far-infrared, which is sensitive to emission from the cooler, outer part of the envelope. We conclude that the best model which describes all the observed infrared and CO data is the one with a density discontinuity, i.e., a superwind surrounded by a tenuous wind. Higher level CO transitions (i.e., $J = 6$–5) probe the temperature structure of the warm gas closer to the star. These lines can be used to distinguish these models.

This work was performed while one of the authors (K. J.) held a National Research Council-NASA ARC Research Associateship. This work is supported, in part (C. J. S.) under the auspices of the U.S. Department of Energy by Lawrence Livermore National Laboratory under contract no. W-7405-ENG-48.

REFERENCES

Arens, J. F., Jernigan, J. G., Ball, R., Peck, M. C., Gaalema, S., & Lacy, J. 1987, in Infrared Astronomy with Arrays, ed. C. G. Wynn-Williams & E. Becklin (Honolulu: Univ. Hawaii), 256
Ball, R., Arens, J. F., Jernigan, J. G., Keto, E., & Meixner, M. 1992, ApJ, 389, 616
Baud, B., & Habing, H. J. 1983, A&A, 127, 73
Bedijn, P. J. 1987, A&A, 186, 136
Bowen, G. H., & Wilson, L. A. 1991, ApJ, 375, L53
Bowers, P. F., & Johnston, K. J. 1990, ApJ, 354, 676
Bowers, P. F., Johnston, K. J., & Spencer, J. H. 1983, ApJ, 274, 733
Cherchneff, I., & Tielens, A. G. G. M. 1994, in Circumstellar Media in Late Stages of Stellar Evolution, Proc. 34th Hertsmonceux Conf., ed. R. E. S. Clegg, I. R. Stevens, & W. P. S. Meikle (Cambridge: Cambridge Univ. Press), 232

Cohen, M., Walker, R. G., Barlow, M. J., Deacon, J. R., Witteborn, F. C., Carbon, D. F., & Augason, G. C. 1995, in IAU Colloq. 136, Stellar Photometry – Current Techniques and Future Development, ed. I. Elliot, in press
Crabtree, D. R., & Rogers, C. 1993, in Second ESO/CTIO Workshop on Mass Loss on the AGB and Beyond, ed. H. E. Schwarz (Munich: ESO), 255
Engels, D., Kreeysa, E., Schultz, G. V., & Sherwood, W. A. 1983, A&A, 124, 123
Evans, N. J., & Beckwith, S. 1977, ApJ, 217, 729
Fix, J. D., & Cobb, M. L. 1988, ApJ, 329, 290
Forrest, W. J., et al. 1978, ApJ, 219, 114
Goldreich, P., & Scoville, N. 1976, ApJ, 205, 144
Griffin, I. P. 1993, MNRAS, 260, 831
Groenewegen, M. A. T. 1994, A&A, 290, 531
Habing, H., Tignon, J., & Tielens, A. G. G. M. 1994, A&A, 286, 523
Haisch, B. M. 1979, A&A, 72, 161
Herman, J., Baud, B., Habing, H. J., & Winnberg, A. 1985, A&A, 143, 122
Herman, J., & Habing, H. 1985, A&AS, 59, 523
Heske, A., Forveille, T., Omont, A., van der Veen, W. E. C. J., & Habing, H. J. 1990, A&A, 239, 173
Iben, I., Jr., & Renzini, A. 1983, ARA&A, 21, 271
Jones, T. J., & Merrill, K. M. 1976, ApJ, 209, 509
Justtanont, K., Skinner, C. J., & Tielens, A. G. G. M. 1994, ApJ, 435, 852
Justtanont, K., & Tielens, A. G. G. M. 1992, ApJ, 389, 400
Kastner, J. 1992, ApJ, 401, 337
Keto, E., Ball, R., Arens, J. F., Jernigan, J. G., & Meixner, M. 1992, International Journal of Infrared and Millimeter Waves, Vol. 13, N11:1709
Knapp, G. R., & Morris, M. 1985, ApJ, 292, 640
Knapp, G. R., Phillips, T. G., Leighton, R. B., Lo, K. Y., Wannier, P. G., Wootten, H. A., & Huggins, P. J. 1982, ApJ, 252, 616
Latter, W. B., Hora, J. L., Kelly, D. M., Deutsch, L. K., & Malony, P. R. 1993, AJ, 106, 1993
Loup, C., Forveille, T., Omont, A., & Paul, J. F. 1993, A&AS, 99, 291
Mamon, G. A., Glassgold, A. E., & Huggins, P. J. 1988, ApJ, 328, 797
Mathis, J. S., Rumpl, W., & Nordsieck, K. H. 1977, ApJ, 217, 425
Meixner, M. 1993, Ph.D. thesis, Univ. California-Berkeley
Netzer, N., & Knapp, G. R. 1987, ApJ, 323, 734
Olofsson, H., Carlström, U., Eriksson, K., Gustafsson, B., & Willson, L. A. 1990, A&A, 230, L13
Olofsson, H., Eriksson, K., Gustafsson, B., & Carlström, U. 1993, ApJS, 87, 267
Renzini, A. 1981, in Physical Processes in Red Giants, ed. I. Iben, Jr. & A. Renzini (Dordrecht: Reidel), 431
Rowan-Robinson, M., & Harris, S. 1983, MNRAS, 202, 767
Sahai, R. 1990, ApJ, 362, 652
Schönberg K., 1985, A&A, 148, 405
———. 1988, A&A, 195, 198
Schönberg, K., & Hempe, K. 1986, A&A, 163, 151
Schönberner, D. 1983, ApJ, 272, 708
Schutte, W., & Tielens, A. G. G. M. 1989, ApJ, 343, 369
Skinner, C. J., et al. 1995, in preparation
Skinner, C. J., & Whitmore, B. 1988, MNRAS, 231, 169
Suh, K. W., Jones, T. J., & Bowen, G. H. 1990, ApJ, 358, 588
Tielens, A. G. G. M. 1983, ApJ, 271, 702
van der Veen, W. E. C. J., Omont, A., Habing, H. J., & Matthews, H. E. 1995, A&A, 295, 445
van Langevelde, H. J., van der Heiden, R., & van Schooneveld, C. 1990, A&A, 239, 193
Vassiliadis, E., & Wood, P. R. 1993, ApJ, 413, 641
Walmsley, C. M., Chini, R., Steppe, H., Forveille, T., & Omont, A. 1991, A&A, 248, 555
Waters, L. B. F. M., Loup, C., Kester, D. J. M., Bontekoe, Tj. R., & de Jong, T. 1994, A&A, 281, L1
Weidemann, V., & Koester, D. 1983, A&A, 121, 77
Werner, M. W., Beckwith, S., Gatley, I., Sellgren, K., Berriman, G., & Whiting, D. L. 1980, ApJ, 239, 540
Wilson, W. J., & Barrett, A. H. 1972, A&A, 17, 385